Liquid Eutectic Gallium-Indium as a Magnesium-Ion Battery Anode with Ultralong Cycle Life Enabled by Liquid–Solid Phase Transformation During (De)Magnesiation at Room Temperature

Journal:	*Journal of Materials Chemistry A*
Manuscript ID	TA-ART-05-2024-003740.R1
Article Type:	Paper
Date Submitted by the Author:	04-Aug-2024
Complete List of Authors:	Wang, Lin; University of Pennsylvania Family, Roxana; University of Pennsylvania, Department of Materials Science & Engineering Ng, Alexander; University of Pennsylvania Detsi, Eric; University of Pennsylvania, Department of Materials Science & Engineering Pikul, James; University of Wisconsin-Madison, Department of Mechanical Engineering

SCHOLARONE™
Manuscripts

Liquid Eutectic Gallium-Indium as a Magnesium-Ion Battery Anode with Ultralong Cycle Life Enabled by Liquid-Solid Phase Transformation During (De)Magnesiation at Room Temperature

Lin Wang,[1] Alexander Ng,[1] Roxana Family,[1] Eric Detsi,[1,*] James Pikul[2,*]

[1] *Department of Materials Science & Engineering, University of Pennsylvania, Philadelphia, PA 19104-6272, USA*

[2] *Department of Mechanical Engineering, University of Wisconsin-Madison, Madison, WI 53705, USA*

[*] *Corresponding authors:* jpikul@wisc.edu *(J. Pikul),* detsi@seas.upenn.edu *(E. Detsi).*

ABSTRACT: Mg-ion batteries represent a promising alternative to Li-ion batteries but face challenges with Mg dendrite formation on Mg metal anodes. Conventional solid alloy anodes prevent Mg dendrite formation but are prone to failure due to significant volume changes during (de)magnesiation. "Self-healing" electrodes composed of liquid alloys can undergo reversible liquid-solid phase transformations during (de)magnesiation, thereby "healing" themselves from the volume expansion-induced material degradation, offering a promising solution. Here, we employ a liquid eutectic Ga-In alloy as a conceptual "self-healing" Mg-ion battery anode with a 246 mAh/g$_{-GaIn}$ theoretical capacity. This anode demonstrates an unprecedented cycle life of 2,000 cycles at the C-rate of 1 C, retaining 91% capacity (225 mAh/g post-cycled capacity) at 25°C. We elucidate the morphology evolution and storage mechanism during (de)magnesiation using *in situ* wide-angle X-ray scattering and cryogenic focused ion beam scanning electron microscopy. These results pave the way for developing high-performance electrodes for next-generation Mg-ion batteries.

Keywords: magnesium-ion battery anode, self-healing, solid-liquid phase transformations, cryogenic focused ion beam, in situ X-ray scattering.

1. Introduction

Mg-ion batteries (MIBs) have emerged as a promising alternative to Li-ion batteries (LIBs) due to Mg metal

being significantly safer, cheaper, and more abundant than Li metals.[1–3] However, MIBs that use Mg metal

anodes face many challenges, including the formation of Mg dendrites at high charging current densities.[4–8]

These Mg dendrites can breach the separator and make direct contact with the cathode, posing a fire hazard.[6]

To overcome these challenges, Mg metal anodes can be replaced with Mg alloy anodes such as Mg-Bi

(capacity: 385 mAh g^{-1} for the Mg_3Bi_2 phase),[9] Mg-Sn (capacity: 903 mAh g^{-1} for the Mg_2Sn phase),[10] Mg-

Sb (capacity: 660 mAh g^{-1} for the Mg_3Sb_2 phase),[11] and Mg-Pb (capacity: 517 mAh g^{-1} for the Mg_2Pb

phase)[12]. However, alloy anodes undergo significant volume changes (up to 300%) and solid-solid phase

transformations during (de)magnesiation, causing severe material pulverization and rapid capacity

decay.[9,10,13] To address these issues, our group recently proposed a novel "self-healing" concept in MIB

electrodes, wherein electrodes continuously "heal" themselves by recovering from volume and phase

change-induced degradation through reversible liquid-solid phase transformations during (de)magnesiation,

unlike the conventional solid-solid phase transformations that occur in solid alloy anodes.[14,15] Our initial

investigations using a standard slurry electrode with solid Mg_2Ga_5 as the active material for Mg storage

demonstrated the benefits of this "self-healing" approach.[14,15] We showed that during (de)magnesiation,

solid Mg_2Ga_5 reversibly transforms into liquid Ga (melting point: 29.5 °C), enabling 1,000 cycles at a current

density of ≈923 mA g^{-1} (equivalent to a C-rate of 3 C) with 80% capacity retention at 40 °C.[15] However,

achieving such performance in the Mg-Ga system at room temperature remains challenging due to solid-

solid phase transformations occurring at room temperature, hindering the "self-healing" process.[14,15]

Eutectic Ga-Sn (EGaSn) alloy can achieve "self-healing" at room temperature or below due to its

relatively low melting point of 20.5 °C.[16] For example, Zhang et al. explored monolithic eutectic Ga-Sn

(EGaSn) films as the anode in MIBs. However, the cycling performance of EGaSn was limited to 250 cycles at a current density of 100 mA g^{-1}.[17–19] Additionally, this current density (100 mA g^{-1}) is roughly 10 times lower than the $\approx$923 mA g^{-1} achieved in the Ga slurry electrode.[15] This limitation arises from the small interfacial area between the monolithic liquid EGaSn electrode film and the electrolyte, which restricts the charge transfer at the electrode/electrolyte interface during (de)magnesiation. Thus, although it is possible to cycle the EGaSn at room temperature, an improved electrode architecture that enhances charge transfer kinetics and further understanding of the underlying liquid-solid phase transformations are needed to achieve extended cycle life and enhanced rate performance. Therefore, in this study, we explore the "self-healing" behavior of liquid eutectic Ga-In alloys (EGaIn, Ga$_{86}$In$_{14}$ at. %) with a melting point of 15 °C (see Fig. S1 for the Ga-In equilibrium phase diagram), and study the electrochemical performance of the EGaIn slurry electrode configuration, which provides a larger active interface area between electrodes and electrolyte to enhance charge transfer kinetics. We use X-ray diffraction (XRD), *in situ* wide-angle X-ray scattering (WAXS), cryogenic focused ion beam scanning electron microscopy (cryo-FIB-SEM), and energy dispersive X-ray spectroscopy (EDS) maps to elucidate the mechanism of liquid-solid phase transformations during (de)magnesiation. Our findings demonstrate the exceptional electrochemical stability of liquid EGaIn slurry electrodes and their ability to sustain 2,000 cycles at the C-rate of 1 C and at room temperature, with 91 % capacity retention (225 mAh g^{-1} post-cycled capacity) at room temperature.

2. Experimental Section

2.1 Preparation of the electrode and electrolyte

Active material: The liquid EGaIn alloy was made by co-melting a stoichiometric amount of Ga (99.99% purity, Fisher Scientific) and In (99.9% purity, Fisher Scientific) at 180 °C for 30 minutes on a hot plate. We

produced the ternary Mg25Ga65In10 at. % alloy by co-melting an off-stoichiometric amount of EGaIn alloy and pure Mg chips (99.98% purity, Sigma-Aldrich) in a graphite boat at 700 °C for 10 minutes in a muffle furnace (KSL-1100X-S-UL-LD, MTI corporation) inside an argon glove box, ensuring safety with heat-resistant gloves. Our composition was off-stoichiometric to compensate for Mg evaporation by adding a 5% excess of Mg.

Slurry electrode: We prepared the slurry electrode by mixing 60 wt. % of Mg25Ga65In10 active material powder with 30 wt. % of conductive carbon mixture (10 wt. % of carbon nanofiber, 10 wt. % of graphene nanosheet, and 10 wt. % of carbon black, Sigma-Aldrich), and 10 wt. % of the binder (polyvinylidene fluoride/N-Methyl-2-pyrrolidone, PVDF/NMP, Sigma-Aldrich). Then, we cast the resulting slurry on a carbon paper current collector and allowed it to dry for 24 hours.

Electrolyte: We prepared the 0.4 M all-phenyl complex (APC) electrolyte by mixing phenyl magnesium chloride (PhMgCl, Sigma-Aldrich) and aluminum chloride ($AlCl_3$, Sigma-Aldrich) with a mass ratio of 2:1 in anhydrous tetrahydrofuran (THF, Sigma-Aldrich) solvent and adding 0.4 M lithium chloride (LiCl) following procedures detailed in our previous works.[13] The LiCl additive's role is to enhance APC's ionic conductivity.[1,21]

All these syntheses were carried out in an argon-filled glove box with water and oxygen content below 0.1 ppm.

2.2 Materials characterization

A Rigaku Miniflex powder diffractometer equipped with a Cu X-ray source was used to collect the XRD patterns at 40 kV, 15 mA, with a step size of 0.01 degrees and a scanning speed of 6 °/min. A JEOL 7500F high-resolution scanning electron microscope with energy dispersive X-ray spectroscopy (EDS, Octane Elect Super detector) was used to collect SEM images and EDS maps for morphology and compositional

analysis. A dual-source Cu/Mo environmental X-ray scattering instrument (Xenocs Xeuss 2.0 at the DEXS facility) was used for *in situ* WAXS studies. A dual-beam plasma Model Tescan S8252X was used to collect cryo-FIB-SEM images at approximately -170 °C.

2.3 Coin cell assembly and electrochemical characterization

Coin cells were assembled inside an argon-filled Mbraun glove box using CR 2032 cell cases. $Mg_{25}Ga_{65}In_{10}$ slurry electrode (with a diameter of 10 mm) was used as the working electrode, a freshly polished Mg foil (MTI Corp.) as the counter and reference electrodes, and 0.4 M APC (containing LiCl) as the electrolyte. The mass loading of the $Mg_{25}Ga_{65}In_{10}$ electrode was ≈2 mg cm^{-2}. We conducted all electrochemical testing using a Bio-Logic potentiostat (Model VMP300). After electrochemical testing, the cycled slurry electrodes were thoroughly washed with a dried THF solvent for subsequent electron microscopy and X-ray characterizations.

3. Results and Discussion

3.1 Liquid-solid phase transformation

Fig. 1a illustrates the reversible liquid-solid phase transformations when Mg is added to or removed from liquid EGaIn. The extent of (de)magnesiation is shown by a red dashed line on the Mg-Ga-In ternary phase diagram in Fig. 1b, generated using FactSage under standard conditions (25 °C and 1 atm). During magnesiation, Mg is introduced into liquid EGaIn, prompting the nucleation and growth of the solid Mg_2Ga_5 phase. The green region of the ternary phase diagram indicates that when the Mg content in liquid EGaIn is less than 7.5 at. %, the system consists of solid Mg_2Ga_5 and liquid Ga-In. When the Mg content in liquid EGaIn ranges from 7.5 to 25 at. %, the system consists of solid Mg_2Ga_5, liquid $Ga_{82}In_{18}$, and solid In, indicated by the blue area in Fig. 1b. The reverse demagnesiation process restores the system to its initial liquid EGaIn state once all Mg has been removed.

To confirm the reversibility of the liquid-solid phase transformation during (de)magnesiation, we used both XRD and *in situ* WAXS techniques to track the phase evolution from the initial solid $Mg_{25}Ga_{65}In_{10}$ to liquid EGaIn after demagnesiation. Fig. 2a shows the typical XRD patterns of the pristine $Mg_{25}Ga_{65}In_{10}$ electrode (purple curve) and the demagnesiated EGaIn electrode (orange curve). The black star (*) indicates the presence of carbon (PDF #26-1080) from the slurry electrode. The XRD of the pristine $Mg_{25}Ga_{65}In_{10}$ electrode confirms the presence of the solid Mg_2Ga_5 phase (PDF #25-0277, green stick pattern), and the solid In phase (PDF #05-0642, the stick pattern). The XRD pattern of the pristine $Mg_{25}Ga_{65}In_{10}$ particles without carbon additives is shown in Fig. 2b. In contrast, the demagnesiated EGaIn electrode only shows carbon peaks without any EGaIn signals. This is expected since liquid EGaIn is amorphous. The disappearance of solid Mg_2Ga_5 and solid In peaks in the XRD pattern of the demagnesiated EGaIn electrode

6

confirms that liquid-solid phase transformation occurs between $Mg_{25}Ga_{65}In_{10}$ and EGaIn electrodes during cycling.

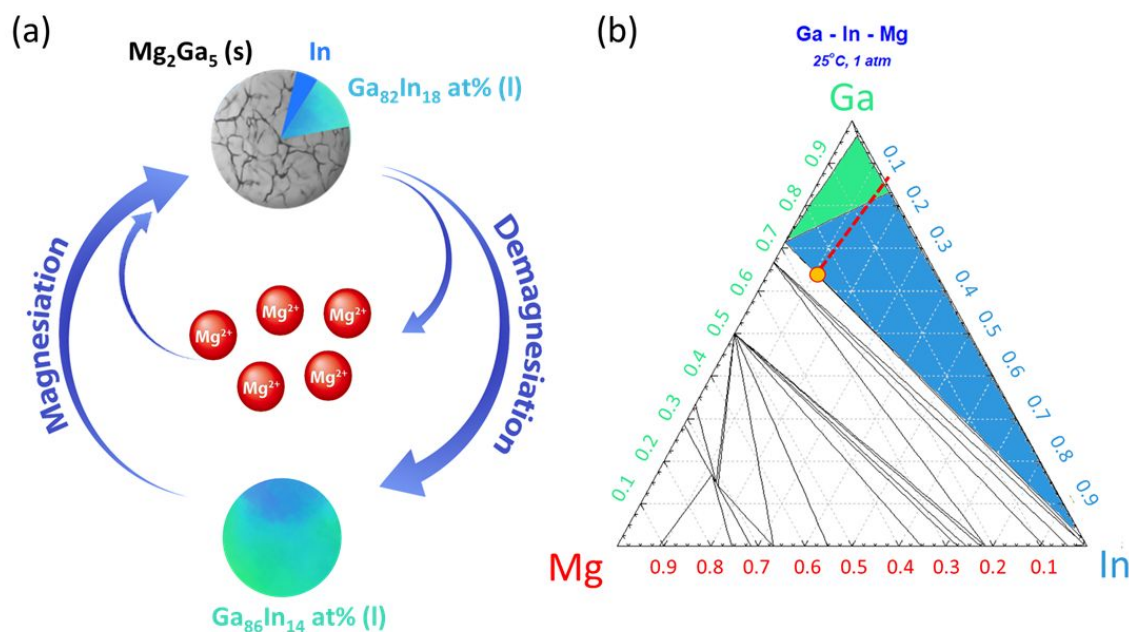**Figure 1.** *(a) Schematic illustration of (de)magnesiation process during which liquid EGain ($Ga_{86}In_{14}$ at. %) is reversibly converted into $Mg_{25}Ga_{65}In_{10}$ (solid Mg_2Ga_5, liquid $Ga_{82}In_{18}$, and solid In). (b) Equilibrium phase diagram of the Mg-Ga-In system at 25 °C and 1 atm generated from FactSage.*

Fig. 2c-e shows the *in situ* WAXS results obtained by cycling the cell within the voltage range of 0.01 to 0.70 V *vs*. Mg/Mg^{2+} at a C-rate of 1 C and at 25 °C. Here, we used a molybdenum X-ray source (Mo Kα, $λ = 0.7094$ Å) and a Linkam heating stage to ensure the testing environment was maintained at 25 °C. Fig. 2c displays the *in situ* WAXS data as the surface plot for three consecutive (de)magnesiation cycles, and the corresponding time vs. voltage curves are shown in Fig. 2d. The dataset in Fig. 2c is normalized against the Mg peak near 15.5°, resulting from the X-ray interaction with the Mg foil (used as the counter and reference electrode). Fig. 2e shows the waterfall plot of *in situ* WAXS result. The green triangles in Fig. 2e represent the standard diffraction peak positions of crystalline Mg_2Ga_5 (PDF #25-0277). The reversible phase

transformation between the solid Mg_2Ga_5 phase and the liquid EGaIn phase during (de)magnesiation is confirmed by the appearance and disappearance of Mg_2Ga_5 peaks at 17.6°, as shown in Figs. 2c and Figs. 2e. Since liquid EGaIn is amorphous, no crystalline peaks related to the formation and disappearance of the liquid EGaIn alloy are observed in the WAXS data. The consistent appearance and disappearance of crystalline Mg_2Ga_5 peaks emphasize the reversible solid-liquid phase transformations during (de)magnesiation.
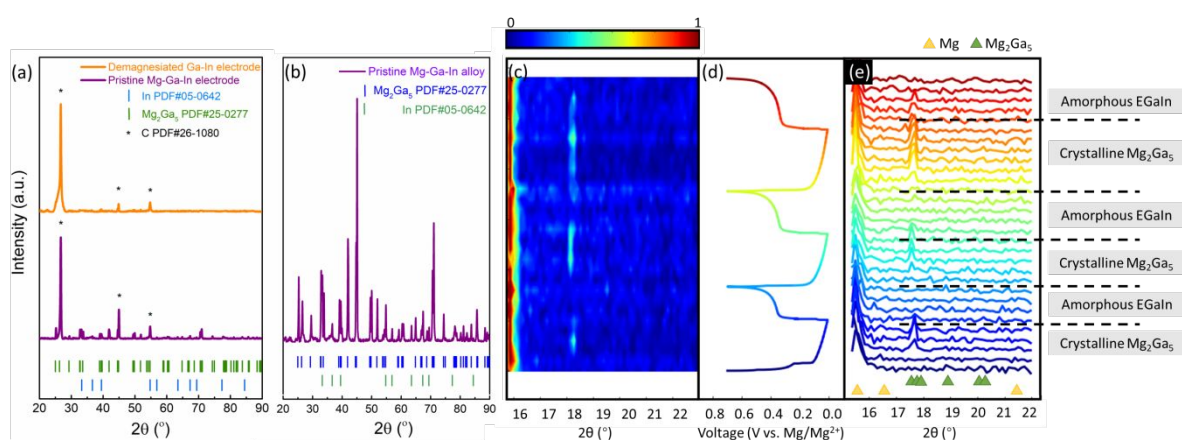

Figure 2. *(a) XRD patterns of the pristine $Mg_{25}Ga_{65}In_{10}$ electrode and the demagnesiated EGaIn electrode. The peaks of carbon additives are indicated by the star (*). (b) XRD patterns of the pristine $Mg_{25}Ga_{65}In_{10}$ particles without carbon additives. (b) Wide-angle X-ray scattering data collected during our cell cycled at 1 C in surface plot. The surface plot in (b) shows the dataset at a higher resolution normalized to the first Mg peak. (c) Voltage curve of our cell cycled at 1 C. The color of the WAXS data in the waterfall plot (d) represents the state of the cell at the time with corresponding color in (c).*

3.2 Electrochemical performance

To study the electrochemical performance of liquid EGaIn slurry electrodes in MIBs, we conducted a comprehensive set of electrochemical tests using the coin cell configuration. Fig. 3a shows the typical cyclic

voltammogram (CV) curves for the following selected cycles: #1, #10, #20, #30, and #50, each distinguished by a different shade of blue. The CV test was conducted in the voltage window between 0.01 and 1.0 V *vs.* Mg/Mg^{2+} at a scan rate of 0.5 mV s^{-1} and 25 °C. The results show two pairs of oxidation/reduction peaks. Each (de)magnesiation process involves two Mg atoms, and each pair corresponds to a slightly different voltage. This is why two oxidation/reduction peaks are observed in the CV curves in Fig. 3a. During the anodic sweep, the two oxidation peaks at 0.30 and 0.41 V correspond to the removal of two Mg atoms from Mg$_2$Ga$_5$ via Equation 1 (forward reaction):

$$\textbf{Mg}_2\textbf{Ga}_5 \rightleftarrows 2\textbf{Mg}^{2+} + 5\textbf{ Ga} + 4\textbf{e}^- \qquad\qquad \textbf{(1)}$$

During the reverse cathodic sweep, the two reduction peaks at 0.16 and 0.07 V indicate the reaction of two Mg atoms with five Ga atoms to form Mg$_2$Ga$_5$ via Equation 1 (reverse reaction).

The long-term cyclability was investigated in galvanostatic mode at the C-rate of 1 C within the voltage range of 0.01 to 0.70 V *vs.* Mg/Mg^{2+} and at 25 °C. At this temperature, EGaIn remains liquid. The cell shows robust electrochemical performance at room temperature, with over 2000 cycles at 1 C. The theoretical capacity is 246 mAh/g-$_{EGaIn}$. After 2,000 cycles, the specific capacity is 225 mAh/g-$_{EGaIn}$ and maintains 91% of its theoretical capacity (the green line in Fig. 3b) with ≈99.94% Coulombic efficiency (the orange line in Fig. 3b). This exceptional cycle life is attributed to two factors: (i) the inherent "self-healing" capability of liquid EGaIn at room temperature, which allows it to recover from potential degradation caused by volume changes through the transition from solid to liquid state as discussed previously;[15] (ii) the use of a slurry electrode (as opposed to a monolithic active material film like the Ga-Sn film discussed in the introduction) ensures that the active material is surrounded by electrolyte, thereby increasing the active interface area between the active material and electrolyte, enabling efficient charge transfer. Fig. 3c presents the galvanostatic charge/discharge curves for the following selected cycles: *#1, #250, #500, #750, #1000,*

#1250, #1500, #1750, and #2000, in different shades of green. The presence of a voltage plateau in these

voltage versus capacity curves supports the Faradaic nature of the charge storage mechanism, as opposed to
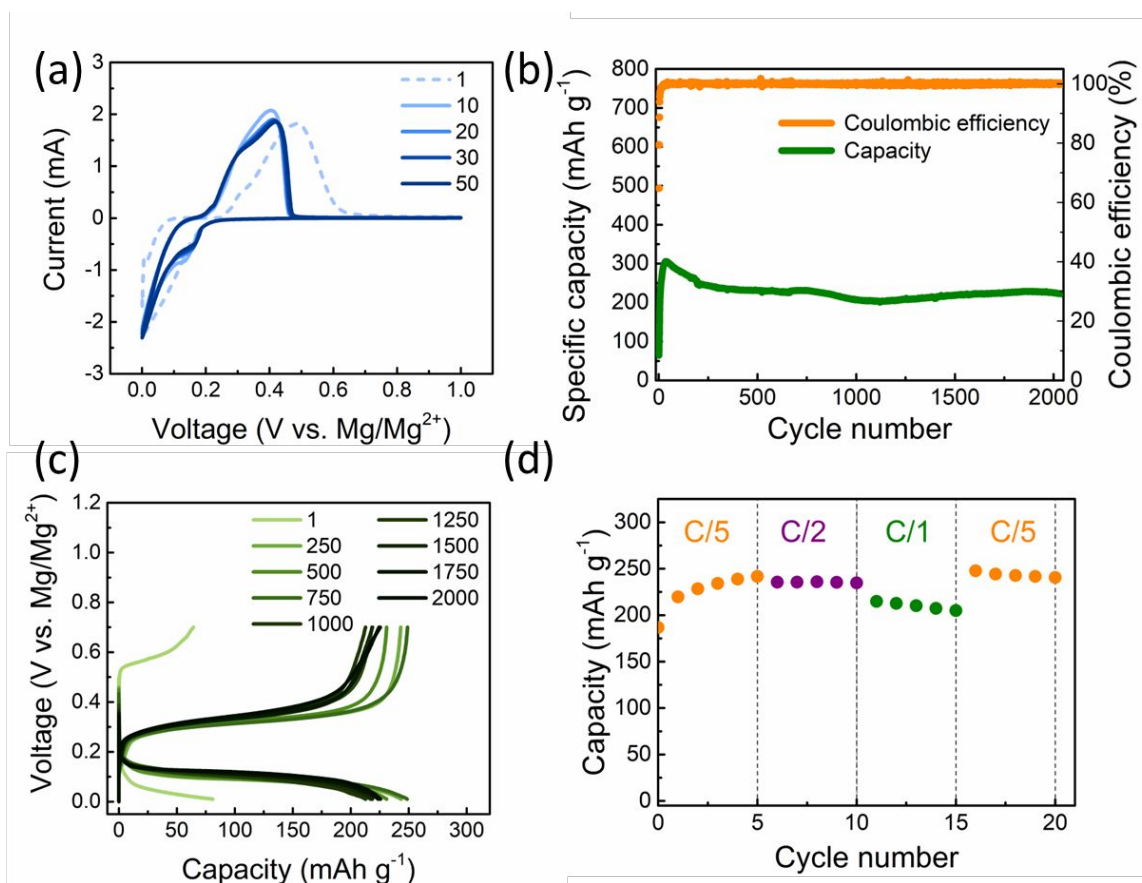
a capacitive one.

Figure 3. *(a) Typical CV curves of the liquid EGaIn slurry electrode in MIBs at a scan rate of 0.5 mV s*

$^{-1}$ at 25 °C. (b) Long-term cycle performance of the liquid EGaIn slurry electrode at 1 C during which

2000 cycles are demonstrated at 25 °C. (c) The corresponding selected galvanostatic charge/discharge

profiles at specific cycles: #1, #250, #500, #750, #1000, #1250, #1500, #1750, and #2000 for the cell

cycled in (b) condition. (d) Rate capability at the C-rates of C/5, C/2, and 1 C.

To understand the rate capability, we cycled the cell at different C-rates from C/5, C/2, 1 C, and back to C/5. Fig. 3d shows the corresponding data. It is observed that the cell delivers a specific capacity of 244 mAh g^{-1} at C/5, 235 mAh g^{-1} at C/2, and 213 mAh g^{-1} at 1 C. Furthermore, the capacity of 244 mAh g^{-1} is fully restored when the cell is cycled at C/5 after being cycled at 1C. The corresponding galvanostatic curves at these different C-rates are presented in Fig. S2. While a consistent voltage plateau is observed in the (de)magnesiation voltage profiles across varied C-rates, there is a noticeable increase in overpotential as the C-rate increases. This is expected, as the charge transfer overpotentials increase with increasing C-rate.

3.3 Morphology and microstructure evolution

To understand the morphology and microstructure evolution during the solid-liquid phase transformation, SEM, EDS mapping, and cryo-FIB-SEM techniques were employed on slurry electrodes before and after demagnesiation. For the pristine $Mg_{25}Ga_{65}In_{10}$ before demagnesiation, the $Mg_{25}Ga_{65}In_{10}$ particles show a rough surface with irregular shapes, as shown in Fig. 4a. The corresponding EDS maps of Mg (yellow, Fig. 4b) and Ga (green, Fig. 4c) reveal an even distribution of Mg and Ga throughout the $Mg_{25}Ga_{65}In_{10}$ particles. The elemental distribution of In (blue in Fig. 4d) demonstrates that some areas overlap with Ga regions, while others exist individually because the pristine $Mg_{25}Ga_{65}In_{10}$ material contains both GaIn and solid In. The EDS results of the pristine $Mg_{25}Ga_{65}In_{10}$ particles are shown in Fig. S3. This insight aligns well with our observations from the Mg-Ga-In ternary phase diagram (Fig. 1b) and the XRD results of the pristine $Mg_{25}Ga_{65}In_{10}$ electrode (Fig. 2a).

After the pristine $Mg_{25}Ga_{65}In_{10}$ electrode was fully demagnesiated, smooth and spherical particles were observed, as shown in Fig. 4e. The EDS map of element Mg (yellow, Fig. 4f) confirms the complete removal of Mg from the active particles, and only element Ga (green, Fig. 4g) and element In (blue, Fig. 4h) are

evenly distributed over the demagnesiated particles. This result also aligns well with our observations from the Mg-Ga-In ternary phase diagram (Fig. 1b) and the XRD results of the pristine $Mg_{25}Ga_{65}In_{10}$ electrode (Fig. 2a).

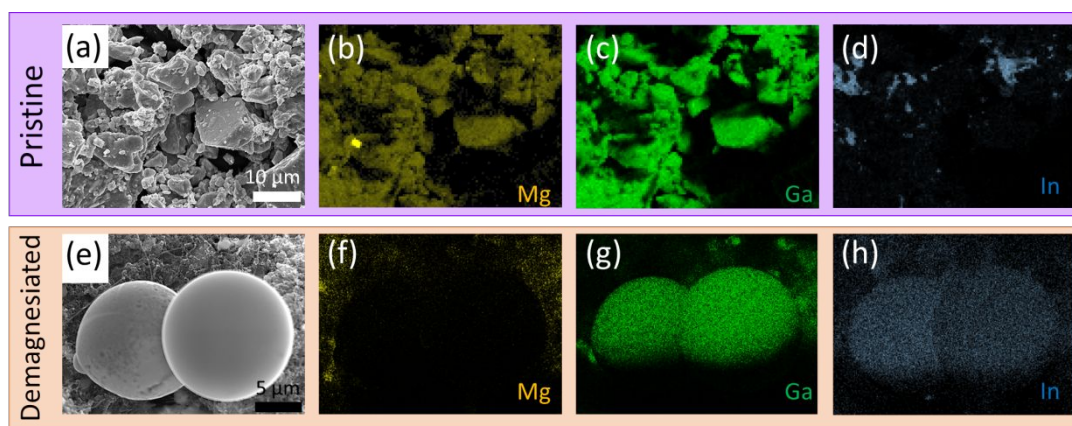**Figure 4.** *SEM images and the corresponding EDS maps of a selected area of (a-d) the pristine Mg25Ga65In10 particles (the purple background), and (e-h) the demagnesiated EGaIn particles (the orange background), embedded in the matrix of a dried composite slurry electrode. EDS maps show the elemental distributions of Mg (yellow), Ga (green), and In (blue) for two electrodes images in (a) and (e), respectively.*

We also used cryo-FIB-SEM with EDS mapping to characterize the internal microstructure of the liquid EGaIn slurry electrode at $\approx$-170 °C. To expose the electrode's cross-section, a large rectangular hole was milled in the demagnesiated EGaIn slurry electrode using a 10 nA Xe-ion plasma FIB milling current at a cryogenic temperature of $\approx$-170 °C. This step was followed by milling with a smaller current of 300 pA to achieve a fine polish and mitigate the curtaining effects.[14] Fig. 5a-c shows a selected cross-sectional area at different magnifications. The contrasting shades—darker and lighter regions—are visually distinguishable due to the differential atomic mass between the carbon-binder matrix phase and the metallic phase.[22] Specifically, the darker regions, identified through the EDS map of the element carbon in blue (shown in

Fig. S4), encompassed carbon additives and binders. In the lighter regions, a homogeneous distribution of

Ga (green in Fig. 5e) and In (blue in Fig. 5f) further confirms the lighter regions as the liquid Ga-In alloy.

The absence of Mg signals (yellow in Fig. 5d) confirms that all Mg has been removed from the active

material after full demagnesiation. Some Ga and In signals are visible in the carbon-based slurry matrix

because the liquid alloy effectively wets the carbon-binder matrix and gradually diffuses through it.[14] This

ensures good contact between the liquid active material (light area) and the surrounding carbon-binder matrix

(dark area), mitigating active material losses and ensuring stable long-term cycling. Meanwhile, the inherent

porous structure of the carbon-binder matrix (as seen in Fig. 5c) enhances electrolyte accessibility to the

active materials. The increased interface between the liquid active material and electrolyte explains the

gradual increase in capacity and Coulombic efficiency observed during the initial cycles in Fig. 3b.
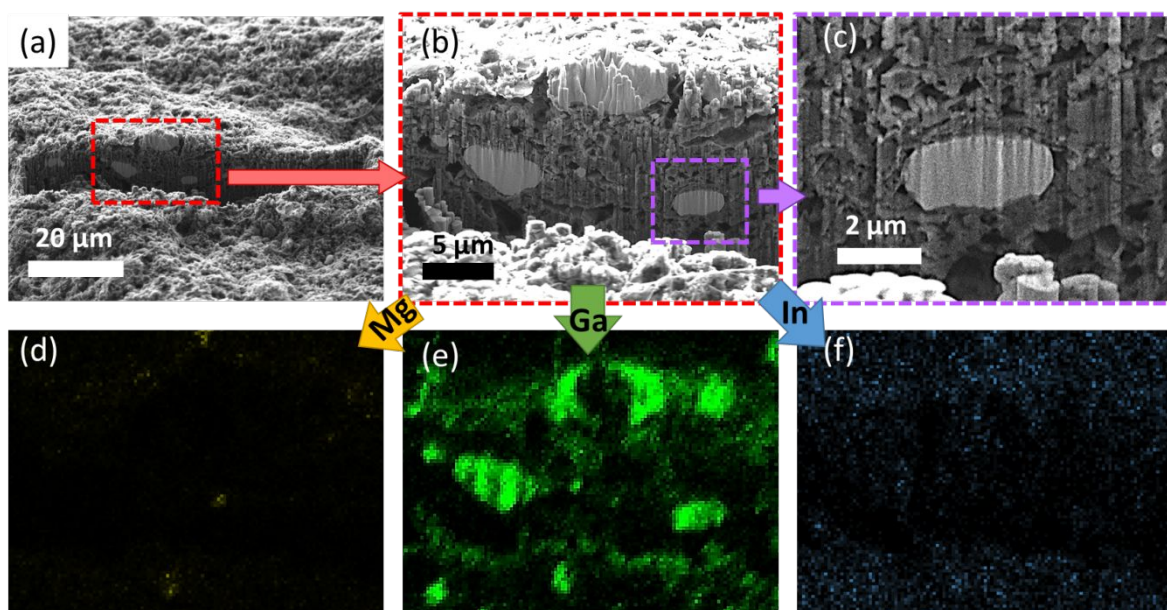
Figure 5. *Cryo-FIB-SEM images with corresponding EDS maps of a demagnesiated EGaIn slurry electrode cross-section area. The selected cross-section area of the demagnesiated EGaIn slurry electrode at (a) a low magnification and (b,c) a higher magnification. The dark phase represents the carbon-biner matrix, while the light phase represents the EGaIn alloy. The corresponding EDS maps show the elemental distribution of (d) magnesium in yellow, (e) gallium in green, and (f) indium in blue.*

3.4 Comparison with state-of-the-art Mg-ion battery anodes

To compare the electrochemical performance of the liquid EGaIn with other anode materials in MIBs, we summarized the results in Fig. 6 and Table S1. [9–13,15,17–19,21,23–33] In Fig. 6, the dots outlined in black represent anodes cycled at room temperature, while triangles outlined in red represent the anodes cycled at elevated temperatures ranging from 40 to 80 °C. The colors of the shapes indicate different cycling current densities: blue for 10 to 99 mA g^{-1}, green for 100 to 499 mA g^{-1}, orange for 500 to 899 mA g^{-1}, and purple for 900 to
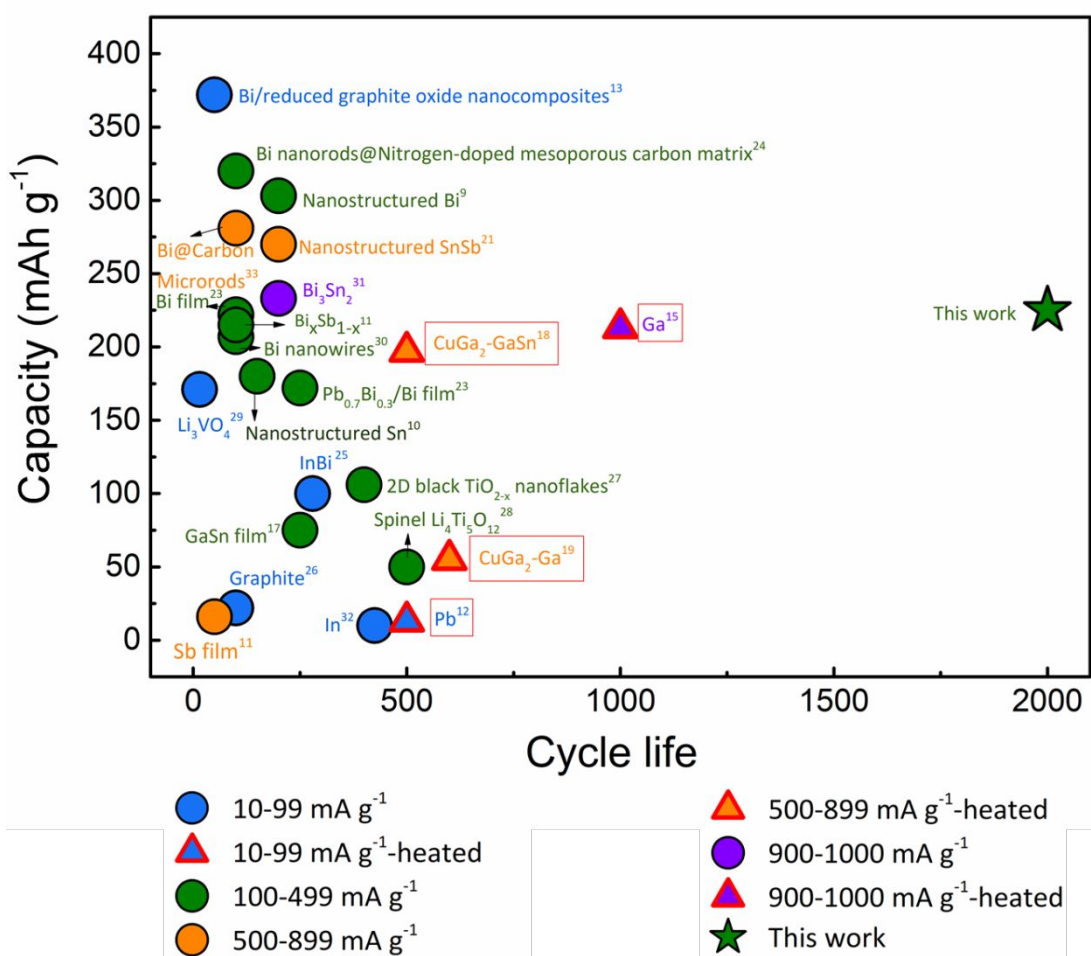

Figure 6. *Comparison of reported anode materials in MIBs in specific capacity, current density, and cycle number.* [9–13,15,17–19,21,23–33] *The shape-filled colors differentiate the cycling current densities, and the shape-outlined colors differentiate the working temperature. The superscript number on each material represents the reference number.*

1000 mA g^{-1}. Among these anode materials, our liquid EGaIn slurry electrode stands out for its longest cycle life and superior post-cycled specific capacity at room temperature. It is worth noting that we excluded the liquid eutectic GaSn alloy film with an intermetallic Ag$_3$Ga compound layer on the stainless steel mesh (ssm-Ag$_3$Ga-EGaSn) anode.[17] The calculated specific capacity of Ag$_3$Ga for magnesium storage is 54.5 mAh g^{-1} (Ag$_3$Ga + Mg $\rightarrow$ Mg$_2$Ga$_5$ + Ag), and the specific capacity of liquid EGaSn is 388 mAh g^{-1} (Ga$_{92}$Sn$_8$ at. % + 44.8 Mg $\rightarrow$ 18.4 Mg$_2$Ga$_5$ + 4 Mg$_2$Sn).[17] However, the reported ssm-Ag$_3$Ga-GaSn anode delivered a capacity exceeding 400 mAh g^{-1}, which surpasses the theoretical limit of its components.

4. Conclusion

In this study, we investigated the use of a liquid EGaIn alloy in slurry electrodes as a conceptual "self-healing" MIB anode that operates at room temperature. The liquid-solid phase transformation occurring during (de)magnesiation at room temperature allows the electrode to "heal" itself, eliminating the need for external heat to maintain its liquid state during cycling. The theoretical capacity of EGaIn is 246 mAh/g$_{-EGaIn}$. Our results demonstrate a remarkable cycle life of 2,000 cycles at a C-rate of 1 C, with 91% capacity retention (225 mAh g^{-1} post-cycled capacity) at room temperature, marking the longest cycle life reported for MIB anodes to date. Using advanced characterization techniques such as *in situ* wide-angle X-ray scattering and cryogenic focused ion beam scanning electron microscopy, we revealed that the exceptional cyclability comes from the synergistic effects of the self-healing capability of liquid EGaIn at room temperature and its chemical wetting behavior on the carbon-binder matrix network. This allows the anode materials to continuously heal themselves from any degradation during cycling, significantly enhancing the cycling life. This conceptual work not only expands the materials landscape but also advances efforts toward more sustainable and efficient energy storage solutions.

Author contributions

L.W. synthesized the materials, performed electrochemical and structural characterizations, and wrote the manuscript; A.N. performed in situ WAXS/electrochemical characterization and contributed to the scientific discussion on in situ WAXS; R.F. contributed to the scientific discussion on Mg electrochemistry, assisted with writing and proofreading the manuscript; J.P. contributed to all scientific discussions, provided guidance, and edited the manuscript; E.D. designed the project and related experiments, oversaw all aspects and direction of the project, and edited the manuscript.

Data Availability Statement

Data and figures for this manuscript are available within the main text and electronic supplementary information.

Conflict of Interest

The authors declare no conflict of interest.

Acknowledgment

References

1.   Yoo, H. D. *et al.* Mg rechargeable batteries: An on-going challenge. *Energy Environ. Sci.* **6**, 2265–2279

        (2013).

2.   Singh, N., Arthur, T. S., Ling, C., Matsui, M. & Mizuno, F. A high energy-density tin anode for

        rechargeable magnesium-ion batteries. *Chem. Commun.* **49**, 149–151 (2013).

3.   Mohtadi, R. & Mizuno, F. Magnesium batteries: Current state of the art, issues and future perspectives.

        Beilstein J. Nanotechnol. **5**, 1291–1311 (2014).

4.   Davidson, R. *et al.* Mapping mechanisms and growth regimes of magnesium electrodeposition at high

        current densities. *Mater. Horizons* **7**, 843–854 (2020).

5.   Zhao, Y. *et al.* Effect of Mg Cation Diffusion Coefficient on Mg Dendrite Formation. *ACS Appl. Mater.*

        Interfaces **14**, 6499–6506 (2022).

6.   Ding, M. S., Diemant, T., Behm, R. J., Passerini, S. & Giffin, G. A. Dendrite Growth in Mg Metal Cells

        Containing Mg(TFSI) 2 /Glyme Electrolytes. *J. Electrochem. Soc.* **165**, A1983–A1990 (2018).

7.   Davidson, R. *et al.* Formation of Magnesium Dendrites during Electrodeposition. *ACS Energy Lett.* **4**,

        375–376 (2019).

8.   Wang, L., Li, P. C. P., Family, R. & Detsi, E. Magnesium dendrite growth during electrodeposition in

        conditioned Mg(TFSI)2/AlCl3/MgCl2/DME electrolyte. *J. Nanoparticle Res.* **26**, 1–7 (2024).

9.   Shao, Y. *et al.* Highly reversible Mg insertion in nanostructured Bi for Mg ion batteries. *Nano Lett.* **14**,

255–260 (2014).

10.   Yaghoobnejad Asl, H. *et al.* In Situ Dealloying of Bulk Mg 2 Sn in Mg-Ion Half Cell as an Effective

       Route to Nanostructured Sn for High Performance Mg-Ion Battery Anodes. *Chem. Mater.* **30**, 1815–1824

       (2018).

11.   Arthur, T. S., Singh, N. & Matsui, M. Electrodeposited Bi, Sb and Bi1-xSbx alloys as anodes for Mg-ion

       batteries. *Electrochem. commun.* **16**, 103–106 (2012).

12.   Periyapperuma, K., Tran, T. T., Purcell, M. I. & Obrovac, M. N. The Reversible Magnesiation of Pb.

       Electrochim. Acta **165**, 162–165 (2015).

13.   Penki, T. R., Valurouthu, G., Shivakumara, S., Sethuraman, V. A. & Munichandraiah, N. In situ synthesis

       of bismuth (Bi)/reduced graphene oxide (RGO) nanocomposites as high-capacity anode materials for a

       Mg-ion battery. *New J. Chem.* **42**, 5996–6004 (2018).

14.   Wang, L., Nelson Weker, J., Family, R., Liu, J. & Detsi, E. Morphology Evolution in Self-Healing Liquid-

       Gallium-Based Mg-Ion Battery Anode. *ACS Energy Lett.* **8**, 4932–4940 (2023).

15.   Wang, L. *et al.* High-Rate and Long Cycle-Life Alloy-Type Magnesium-Ion Battery Anode Enabled

       Through (De)magnesiation-Induced Near-Room-Temperature Solid–Liquid Phase Transformation. *Adv.*

       Energy Mater. **9**, 1–7 (2019).

16.   Song, M. & Zhang, Z. Self-healing Ga-based liquid metal/alloy anodes for rechargeable batteries. *Nano*

       Res. (2023) doi:10.1007/S12274-023-5955-9.

17.   Song, M. *et al.* A high-performance room-temperature magnesium ion battery with self-healing liquid

       alloy anode mediated with a bifunctional intermetallic compound. *Chem. Eng. J.* **450**, 138176 (2022).

18.   Song, M. *et al.* A self-healing room-temperature liquid eutectic GaSn anode with improved wettability

       for advanced Mg ion batteries. *Chem. Eng. J.* **435**, 134903 (2022).

19. Song, M., Niu, J., Cui, W., Bai, Q. & Zhang, Z. Self-healing liquid Ga-based anodes with regulated wetting and working temperatures for advanced Mg ion batteries. *J. Mater. Chem. A* **9**, 17019–17029 (2021).

20. Wang, Z. *et al.* Degradation of magnesium-ion battery anodes by galvanic replacement reaction in all-phenyl complex electrolyte. *J. Energy Storage* **23**, 195–201 (2019).

21. Cheng, Y. *et al.* Interface Promoted Reversible Mg Insertion in Nanostructured Tin-Antimony Alloys. *Adv. Mater.* **27**, 6598–6605 (2015).

22. Lee, T., Corsi, J. S., Wang, L. & Detsi, E. Air-Stable Nanoporous Aluminum/Lithium Borohydride Fuel Pellets for Onboard Hydrogen Generation by Hydrolysis with Pure Water. *ACS Appl. Energy Mater.* (2021) doi:10.1021/acsaem.1c01825.

23. Cen, Y. *et al.* Bi nanorods anchored in N-doped carbon shell as anode for high-performance magnesium ion batteries. *Electrochim. Acta* **397**, 139260 (2021).

24. Liu, Z. *et al.* Insights into the electrochemical performances of Bi anodes for Mg ion batteries using 25Mg solid state NMR spectroscopy. *Chem. Commun.* **53**, 743–746 (2017).

25. Song, M. *et al.* Phase engineering in lead-bismuth system for advanced magnesium ion batteries. *J. Mater. Chem. A* **8**, 13572–13584 (2020).

26. Niu, J. *et al.* Composition- and size-modulated porous bismuth-tin biphase alloys as anodes for advanced magnesium ion batteries. *Nanoscale* **11**, 15279–15288 (2019).

27. Murgia, F., Monconduit, L., Stievano, L. & Berthelot, R. Electrochemical magnesiation of the intermetallic InBi through conversion-alloying mechanism. *Electrochim. Acta* **209**, 730–736 (2016).

28. Murgia, F., Weldekidan, E. T., Stievano, L., Monconduit, L. & Berthelot, R. First investigation of indium-based electrode in Mg battery. *Electrochem. commun.* **60**, 56–59 (2015).

29. Wang, Y. *et al.* Atomic Substitution Enabled Synthesis of Vacancy-Rich Two-Dimensional Black TiO 2-x Nanoflakes for High-Performance Rechargeable Magnesium Batteries. *ACS Nano* **12**, 12492–12502 (2018).

30. God, C. *et al.* Intercalation behaviour of magnesium into natural graphite using organic electrolyte systems. *RSC Adv.* **7**, 14168–14175 (2017).

31. Zeng, J. *et al.* Li3VO4: an insertion anode material for magnesium ion batteries with high specific capacity. *Electrochim. Acta* **247**, 265–270 (2017).

32. Wu, N. *et al.* A highly reversible, low-strain Mg-ion insertion anode material for rechargeable Mg-ion batteries. *NPG Asia Mater.* **6**, 1–7 (2014).

33. Zhang, F., Shen, Y., Xu, H. & Zhao, X. Bismuth Nanoparticle-Embedded Carbon Microrod for High-Rate Electrochemical Magnesium Storage. *ACS Appl. Mater. Interfaces* **15**, 23353–23360 (2023).

Data Availability Statement

Data and figures for this manuscript are available within the main text and electronic supplementary information.